NMR investigations of dynamical tunneling in spin systems

V. R. Krithika,[1,2,*] M. S. Santhanam,[1,†] and T. S. Mahesh[1,2,‡]
[1]*Department of Physics, Indian Institute of Science Education and Research, Pune 411008, India*
[2]*NMR Research Center, Indian Institute of Science Education and Research, Pune 411008, India*

(Received 19 May 2023; accepted 28 August 2023; published 8 September 2023)

In the usual quantum tunneling, a low-energy quantum particle penetrates across a physical barrier of higher potential energy, by traversing a classically forbidden region, and finally escapes into another region. In an analogous scenario, a classical particle inside a closed regular region in the phase space is dynamically bound from escaping to other regions of the phase space. Here, the physical potential barrier is replaced by dynamical barriers which separate different regions of the phase space. However, in the quantum regime, the system can overcome such dynamical barriers and escape through them, giving rise to *dynamical tunneling*. In chaotic Hamiltonian systems, dynamical tunneling refers to quantum tunneling between states whose classical limits correspond to symmetry-related regular regions separated by a chaotic zone between which any classical transport is prohibited. Here, an experimental realization of dynamical tunneling in spin systems is reported using nuclear magnetic resonance (NMR) architecture. In particular, dynamical tunneling in quantum kicked tops of spin-1 and spin-3/2 systems using two- and three-qubit NMR registers is investigated. By extracting time-dependent expectation values of the angular momentum operator components, size-dependent tunneling behavior for various initial states is systematically investigated. Further, by monitoring the adverse effects of dephasing noise on the tunneling oscillations, we assert the importance of quantum coherence in enabling dynamical tunneling.

DOI: 10.1103/PhysRevA.108.032207

I. INTRODUCTION

Quantum tunneling usually refers to the phenomenon by which a wave packet penetrates and transits through a physical potential barrier despite having lesser energy than the barrier height [1]. Classically, this is a forbidden process, though it is allowed in a quantum system. The quantum tunneling phenomenon has been studied extensively and has found applications in various fields ranging from nuclear physics, superconductivity, and electronics to microscopy [1–8].

In chaotic Hamiltonian systems, quantum tunneling manifests into a much richer and more complex phenomenon due to the complexity of underlying classical dynamics [9,10]. Interestingly, it was realized that the quantum tunneling phenomenon can be extended to scenarios even without any physical barrier. In such cases, the potential barriers are replaced by dynamical barriers formed by invariant phase space structures in the classical limit. Hence, this is often called dynamical tunneling. It was first recognized in experimentally determined local mode doublets of H_2O [11,12], and extensively studied by Davis and Heller (see Refs. [13,14]) in a two-dimensional nonlinear system. Dynamical tunneling happens when a wave packet tunnels between symmetry-related regular regions such as elliptic islands. It is important to note that the regular regions are separated, not necessarily by potential barriers, but by dynamical constraints. A classical particle initialized in one such regular region can never couple with the other, and hence any transport between these regions is forbidden. In a semiclassical sense, these regular regions would contribute to degenerate eigenstates. However, if tunneling is present between these regular classical regions, we expect the disconnected classical regions to be coupled by quantum dynamics and the degeneracy is lifted. This results in characteristic tunneling doublets in the energy spectrum. The corresponding eigenstates are symmetric and antisymmetric linear combinations of wave functions that predominantly localize on these regular regions [7,9,13,15,16]. This can be effectively modeled as a two-state process (a two-level system) involving these nearly degenerate states.

It was found that the tunneling rate between the regular regions can be further enhanced if these regions are separated by a sea of chaos [9]. In this case, the tunneling wave function has an overlap also with the chaotic region, which aids the tunneling process. In this case dynamical tunneling, termed as chaos-assisted tunneling, is a process involving three levels—the two nearly degenerate states coupled through an intermediate chaotic state. The chaotic state can be modeled as a typical state drawn from an appropriate random matrix ensemble. It must be pointed out that a similar mediation by the classical nonlinear resonances, called the resonance assisted tunneling, in the near-integrable regime also leads to enhanced tunneling rates between low and high excited states lying within the same nonlinear resonance region [17–23]. This phenomenon was also reported in a system with three degrees of freedom [24]. The rate of tunneling in integrable systems comparatively is much slower due to the absence of resonances and chaos. It is evident that quantum tunneling behavior can be strongly influenced by the underlying

*krithika_vr@students.iiserpune.ac.in
†santh@iiserpune.ac.in
‡mahesh.ts@iiserpune.ac.in

classical structures arising from integrability and nonintegrability of the system [10,16,25].

Though dynamical tunneling has been theoretically explored for the last three decades, experimental demonstrations are far fewer [9,26–34]. They are limited to essentially two chaotic testbeds, namely, a driven cold atomic cloud [27,29,30] and microwave annular billiards [26,31]. Despite the popularity of kicked models within the fold of quantum chaos, especially the ones based on spins such as the kicked top model [35], only one experimental demonstration until now has employed kicked systems [36]. A theoretical study of dynamical tunneling in the quantum kicked top (QKT) had been reported in Refs. [37,38]. Reference [37] showed that in the presence of dynamical tunneling between regular regions, the expectation values of angular momentum operator components display periodic revivals. To our knowledge, this feature has not been explicitly shown through experiments so far.

Nuclear magnetic resonance (NMR) has been a convenient testbed for quantum simulations and development of methodologies for quantum information processing [39,40]. Previous NMR studies of nonlinear dynamics include investigating bifurcation in a quadrupolar NMR system [41], realizing QKT with nuclear spin qubits [42], phase synchronization in a pair of interacting nuclear spins subjected to an external drive [43], quantum phase transitions [44–46], out-of-time-order correlations in integrable and nonintegrable systems [47], etc. In this paper, we carry out NMR investigation of dynamical tunneling in a QKT model formulated as a collection of periodically kicked and interacting spins. This model is useful because the approach to the classical limit can be attained by expanding the Hilbert space, by either increasing the number of spins, or the spin number, or both. Hence, this system provides a convenient route to study dynamical tunneling and push it towards the classical limit. By monitoring the expectation values of the angular momentum operators of the QKT, we performed a systematic experimental investigation into (i) dynamical tunneling in spin systems for different initial states, (ii) system size dependence of tunneling period with two different system sizes, and (iii) effect of dephasing noise on the robustness of tunneling. By observing the prolonged time periods of dynamical tunneling in the larger system, we infer the inverse size dependence of the phenomenon. The dephasing noise also resulted in dampening of tunneling amplitudes, which incidentally appears to have relatively stronger effects on the larger system.

The paper is organized as follows. We introduce the QKT model and the concept of dynamical tunneling in spin systems in Sec. II. We explain the methodologies of NMR experiments in Sec. III, followed by results in Sec. IV, and finally conclude in Sec. V.

II. DYNAMICAL TUNNELING IN SPIN SYSTEMS

A. Quantum kicked top model

The QKT model of a spin-j system is described by the Hamiltonian (with $\hbar$ set to unity) [35,37]

$$H_{\mathrm{QKT}} = \frac{\pi}{2} J_y \sum_n \delta(t - n\tau) + \frac{k}{2j} J_z^2, \tag{1}$$

where J_α with $\alpha = x, y, z$ are components of the angular momentum operator. The first term describes an instantaneous kick about the y axis which brings about a rotation of $\pi/2$ angle, and the second term characterized by the chaoticity parameter k describes a nonlinear torsion about the z axis. However, in experiments, we cannot realize ideal instantaneous δ kicks, but only kicks of finite widths. Hence, the above equation for kicks of finite width can be expressed as

$$H_{\mathrm{QKT}} = \begin{cases} H_{\mathrm{kick}} = \frac{\pi}{2\Delta} J_y, & \text{for } t \in \left[n\tau - \frac{\Delta}{2}, n\tau + \frac{\Delta}{2}\right] \\ H_{\mathrm{NL}} = \frac{k}{2j\tau} J_z^2, & \text{otherwise} \end{cases}. \tag{2}$$

Here, Δ is the kick duration that produces a $\pi/2$ rotation about the y axis described by the unitary operator $U_{\mathrm{kick}} = \exp\{-iH_{\mathrm{kick}}\Delta\}$. The second term describes the nonlinear evolution governed by the chaoticity parameter k for a time period τ with the corresponding unitary $U_{\mathrm{NL}} = \exp\{-iH_{\mathrm{NL}}\tau\}$. The effective Floquet operator can then be written as $\mathcal{U} = U_{\mathrm{NL}} U_{\mathrm{kick}}$. The dynamics of the system can be evaluated from the evolution of angular momentum components of the QKT under the Floquet evolution after the nth kick as $J_\alpha(n+1) = \mathcal{U}^\dagger J_\alpha(n)\mathcal{U}$, for $\alpha = \{x, y, z\}$. The classical map can be obtained from the scaled variables $V = J_\alpha/j$ in the limit $j \to \infty$ [35] which leads to the following equations of motion:

$$\begin{aligned} X' &= Z\cos(kX) + Y\sin(kX), \\ Y' &= -Z\sin(kX) + Y\cos(kX). \\ Z' &= -X. \end{aligned} \tag{3}$$

Since the total angular momentum of the system is conserved, the dynamics of the system can be parametrized in terms of two parameters (θ, ϕ) such that $X = \sin\theta\cos\phi$, $Y = \sin\theta\sin\phi$, $Z = \cos\theta$. For low values of the chaoticity parameter, $k \approx 0.5$, the system is highly regular, but it transitions to a mixed phase space as k is increased before becoming almost completely chaotic at around $k = 6$ [48]. This map has time-reversal symmetry and reflection symmetry about the y axis [35]. The classical phase space for $k = 3$ is shown in Fig. 1. Under classical evolution, even as time $t \to \infty$, the initial conditions indicated by **A** and **A**′ in Fig. 1 will remain trapped in their respective regular regions. However, if the system is initialized in a chaotic region, indicated by **C** in Fig. 1, it can then explore the entire connected chaotic layer of the phase space. In contrast, a QKT initialized in one of the regular regions can tunnel to other regular regions, giving rise to dynamical tunneling, as explained below.

B. Dynamical tunneling in the QKT model

Just as a wave packet can tunnel through a potential barrier with higher energy, quantum systems can overcome *dynamical barriers* and couple regular regions which are classically disconnected and between which any classical transport is strictly forbidden. A classical system initialized in one of the regular regions, **A** and **A**′ in Fig. 1, remains localized, while a quantum system can defy the classical dynamical barrier and periodically tunnel to and from the other regular region of appropriate symmetry [15]. Such periodic tunneling behavior was theoretically studied in Ref. [37] using the QKT model for a spin $j = 18$ system.

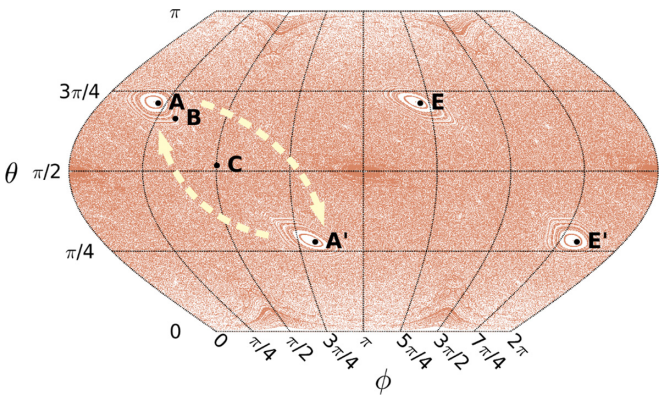

FIG. 1. Classical phase space of the kicked top model for chaoticity parameter $k = 3$. The mixed phase space has distinct regular islands separated by a chaotic sea. A classical system initialized in the regular regions, labeled by **A** and **A**′, will continue to remain there throughout the dynamics, while that initialized in the near-regular region, labeled by **B**, can move along its periodic orbit, and that initialized in the chaotic region, labeled by **C**, can explore the phase space. The regions labeled by **E** and **E**′ form a period-2 orbit and keep jumping from one to the other with every kick. The dynamics of a QKT initialized in the states **A**, **B**, and **C** studied here reveal dynamical tunneling between **A** and **A**′ as indicated by the arrows.

The tunneling phenomenon was captured using the expectation values $\langle J_\alpha \rangle$ of the scaled angular momentum operator J/j. Periodic revivals in expectation values of $\langle J_\alpha \rangle$ indicated tunneling between regular regions, while lack of clear oscillations indicated absence of tunneling. Interestingly, a QKT initialized in a regular region showed clear periodicity, while that initialized in a chaotic region did not show such clear periodicity.

While our experiments use the same QKT model, we first numerically study the system size dependence of tunneling behavior for chaoticity parameter $k = 3$. As the system size increases ($j \to \infty$), the classical limit is approached, and the tunneling behavior is suppressed. Let us consider the initial state $\mathbf{A} \equiv |\theta_\mathbf{A}, \phi_\mathbf{A}\rangle \equiv (2.25, 0.63)$ at the center of one of the regular regions and its symmetry related state $\mathbf{A}' \equiv \exp(-i\pi J_y)|\theta_\mathbf{A}, \phi_\mathbf{A}\rangle \equiv (\pi - 2.25, \pi - 0.63)$ (see Fig. 1). The numerical simulations of $\langle J_\alpha \rangle$ for the QKT model for different spin sizes starting from **A** are shown in Figs. 2(a)–2(c). It is clear that $\langle J_x \rangle$ and $\langle J_z \rangle$ show rapid oscillations for $j = 1$ [Fig. 2(a)] indicating tunneling between **A** and **A**′. However, for a larger system with $j = 10$ [Fig. 2(b)] the period is elongated, and for $j = 100$ [Fig. 2(c)] the system shows no sign of periodicity in the chosen time range. It is interesting to note that the other two similar-looking regular regions, labeled by $\mathbf{E} \equiv |\theta_\mathbf{E}, \phi_\mathbf{E}\rangle = (2.25, 0.63 + \pi)$ and $\mathbf{E}' \equiv \exp(-i\pi J_y)|\theta_\mathbf{E}, \phi_\mathbf{E}\rangle \equiv (\pi - 2.25, 2\pi - 0.63)$, have a totally different behavior, as shown in Figs. 2(d)–2(f). They form a period-2 orbit and oscillate between one another with every kick in the classical limit [35]. This is clearly observed for a large spin system, such as $j = 100$ in Fig. 2(f). For smaller spin sizes, such as $j = 1$ and 10 [Figs. 2(d) and 2(e)], the values of $\langle J_x \rangle$ and $\langle J_z \rangle$ show irregular oscillations with beat patterns.

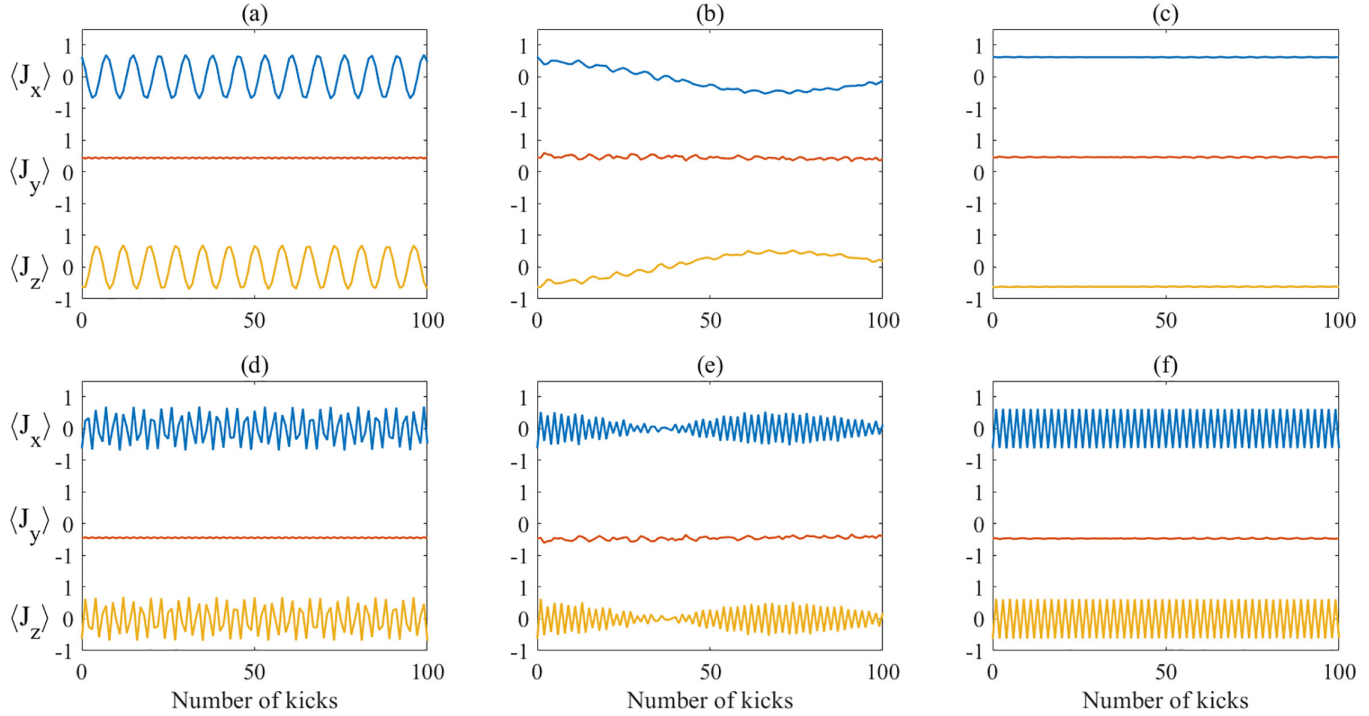

FIG. 2. Normalized expectation values of angular momentum operator components $\langle J_\alpha \rangle$ obtained from numerical simulations with $k = 3$ starting from the states **A** (a)–(c) and **E** (d)–(f) for spin sizes $j = 1$ (a), (d), $j = 10$ (b), (e), and $j = 100$ (c), (f). As the spin size increases the system tends towards the classical limit exhibiting prolonged tunneling periods. For the latter initial state (d)–(f), the oscillations in expectation values $\langle J_\alpha \rangle$ are maintained for all spin sizes, with the system exhibiting clear period-2 oscillations as it tends to the classical limit, which can be seen prominently for $j = 100$ (f).

(a) Sodium fluorophosphate

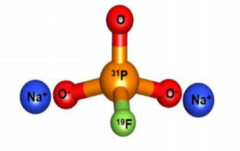

^{19}F	^{31}P	(Hz)	T_1 (s)	T_2^* (s)
0	868	^{19}F	4.4	0.3
	0	^{31}P	6.7	0.4

(b) Dibromofluoromethane

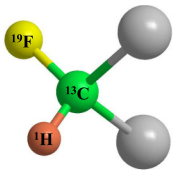

^{13}C	^{1}H	^{19}F	(Hz)	T_1 (s)	T_2^* (s)
0	224.5	-311.1	^{13}C	2.4	0.3
	0	49.7	^{1}H	12.6	0.4
		0	^{19}F	7.2	0.2

FIG. 3. Experimental systems used for tunneling experiments. (a) The two-qubit system of sodium fluorophosphate used to simulate a single spin-1 system and (b) three-qubit system of dibromofluoromethane used to simulate a single spin-3/2 system, along with their Hamiltonian parameters shown in the tables below. The diagonal elements indicate resonance offsets, while off-diagonal elements indicate the scalar $\mathcal{J}$-coupling constant values in Hz. Also shown are the T_1 and T_2^* values of the different nuclear species.

III. EXPERIMENTAL METHODOLOGY

A. NMR Hamiltonian

To study the size dependent behavior of dynamical tunneling, we simulated the QKT in spin-1 and spin-3/2 systems using two- and three-qubit NMR systems respectively. The two-qubit system was composed of ^{19}F and ^{31}P of sodium fluorophosphate [Fig. 3(a)] dissolved in D_2O, and the three-qubit system was composed of ^{13}C, ^{1}H, and ^{19}F spins of dibromofluoromethane [Fig. 3(b)] dissolved in deuterated acetone. All the experiments were performed on samples containing about 10^{15} nuclear spins maintained at 300 K on a Bruker 500-MHz high-resolution spectrometer with a static magnetic field $B_0\hat{z}$ with $B_0 = 11.7$ T. The field lifts the degeneracy of m_s spin levels via the Zeeman interaction, with an energy gap $\hbar\gamma_i B_0$ which has the corresponding Larmor frequency of $\omega_i = \gamma_i B_0$ where γ_i is the gyromagnetic ratio of the spin [49]. Different nuclear spin species exist in different chemical environments which influence the effective field experienced by the spins. The resulting time-averaged local field corresponds to a modified Larmor frequency $\omega_i = \gamma_i B_0(1+\delta_i)$, where δ_i is the chemical shift of the spins [49]. The spins also interact indirectly with one another via the scalar coupling constant $\mathcal{J}_{ij}$ mediated by covalent bonds. For the heteronuclear systems considered here, we move to a rotating frame resonant with the Larmor frequencies of the spins and the resonance offsets may be set to zero [49]. The effective NMR Hamiltonian in the weak-coupling limit is then given only by the scalar $\mathcal{J}_{ij}$ coupling interaction and takes the form [49]

$$H_{\mathcal{J}} = \sum_{i,j>i} 2\pi \mathcal{J}_{ij} I_{zi} I_{zj}. \tag{4}$$

The spins can further be manipulated by radio-frequency (rf) pulses resonant with the corresponding characteristic Larmor frequencies and described by the Hamiltonian

$$H_{\rm rf} = \sum_i \frac{\pi}{2\Delta_i} I_{yi}, \tag{5}$$

where Δ_i is the pulse duration corresponding to the ith spin species. Hence the NMR system with the rf pulses is described by the combined Hamiltonian [42]

$$H_{\rm NMR} = \sum_i \frac{\pi}{2\Delta_i} I_{yi} + \sum_{i,j>i} 2\pi \mathcal{J}_{ij} I_{zi} I_{zj}. \tag{6}$$

In systems with three or more qubits, we can realize a uniform evolution under a single effective scalar coupling constant $\mathcal{J}$ by using the standard spin echo methods [50], such that

$$\begin{aligned} H_{\rm NMR}^{\rm eff} &= H_{\rm rf} + H_{\mathcal{J}}^{\rm eff} \\ &= \sum_i \frac{\pi}{2\Delta_i} I_{yi} + \mathcal{J} \sum_{i,j>i} 2\pi I_{zi} I_{zj}. \end{aligned} \tag{7}$$

Comparing this with Eq. (2), we can see that the linear term $H_{\rm kick}$ can be mapped to the rf term $H_{\rm rf}$. Since we realize the spin-j QKT using a collection of $2j$ qubits [48,51], the nonlinear term in Eq. (2) can be expanded as

$$\begin{aligned} \frac{k}{2j\tau} J_z^2 &= \frac{k}{2j\tau} \left(\sum_{i=1}^{2j} I_{zi} \right)^2 \\ &= \frac{k}{2j\tau} \left[\sum_{i=1}^{2j} I_{zi}^2 + 2 \sum_{i=1,j>i}^{2j} I_{zi} I_{zj} \right] \\ &= \frac{k}{2j\tau} \left[\sum_{i=1}^{2j} \frac{\mathbb{1}}{4} + 2 \sum_{i=1,j>i}^{2j} I_{zi} I_{zj} \right] \\ &\equiv \frac{k}{2j\tau} 2 \sum_{i=1,j>i}^{2j} I_{zi} I_{zj}. \end{aligned} \tag{8}$$

Thus, the nonlinear term can be mapped to the scalar $\mathcal{J}$ coupling term $H_{\mathcal{J}}^{\rm eff}$ up to the identity term which only introduces an unobservable global phase. Moreover, comparing Eq. (8) with $H_{\mathcal{J}}^{\rm eff}$, we can see that $k = 2j\pi\mathcal{J}\tau$, which enables us to vary the chaoticity parameter k by tuning the duration τ of the effective $\mathcal{J}$ evolution. Since the duration of the rf pulse $\Delta_i \ll \tau = k/(2j\pi\mathcal{J})$, we ignore $H_{\mathcal{J}}^{\rm eff}$ during the rf pulse and hence decompose the Floquet evolution $\mathcal{U}_{\rm NMR} = U_{\mathcal{J}} U_{\rm rf}$, where $U_{\rm rf} = \exp(-iH_{\rm rf}\Delta)$ and $U_{\mathcal{J}} = \exp(-iH_{\mathcal{J}}^{\rm eff}\tau)$.

B. Initial-state preparation

At ambient temperatures, the thermal energy $k_B T$ of the NMR spin system is much larger than the Zeeman energy splitting $\hbar\gamma_i B_0$. Hence, an n-qubit system is in a highly mixed state and is given by the Boltzmann distribution [49]

$$\rho_{\rm eq} \simeq \frac{\mathbb{1}}{2^n} + \sum_i \epsilon_i I_{zi}, \tag{9}$$

where $\mathbb{1}/2^n$ captures the uniform population background, and the purity factor $\epsilon_i = \hbar\gamma_i B_0/(2^n k_B T) \approx 10^{-5}$ captures the deviation from uniform population distribution.

To simulate the dynamics of a QKT, it is conventional to initialize the system into coherent states as these are closest to a classical state [52,53]. We simulate a spin-j QKT using $2j$

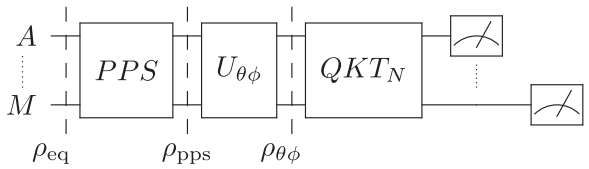

FIG. 4. An experimental circuit to realize the QKT model in a system of M qubits. Starting from the state $\rho_{\rm eq}$ in thermal equilibrium, a pseudopure state $\rho_{\rm PPS}$ is prepared. This is followed by preparation of initial state $\rho_{\theta\phi}$. We then implement the QKT model for N kicks and finally read out each qubit.

qubits initialized in the spin coherent state defined as

$$|\theta,\phi\rangle = U_{\theta\phi}|0\rangle^{\otimes n}, \quad \text{where } U_{\theta\phi} = e^{-i\phi\sum_i I_{zi}} e^{-i\theta\sum_i I_{yi}}. \tag{10}$$

To realize this in a multiqubit NMR spin system, we first transform the thermal equilibrium state $\rho_{\rm eq}$ to a pseudopure (PPS) state of the form $\rho_{\rm PPS} = (1-\epsilon)\mathbb{1}/2^n + \epsilon|\psi\rangle\langle\psi|$ whose dynamics can be mapped isomorphically to the dynamics of a pure state $|\psi\rangle$ [54,55]. The detailed NMR pulse sequences for preparing PPS of the two- and three-qubit spin systems considered here are given in Ref. [56]. These states can then further be transformed into coherent states $|\theta,\phi\rangle$ for an n-qubit system:

$$\rho_{\theta\phi} = U_{\theta\phi}\rho_{\rm PPS}U_{\theta\phi}^{\dagger} \equiv |\theta,\phi\rangle\langle\theta,\phi|. \tag{11}$$

The system is thus initialized to a required (θ,ϕ) coordinate in the phase space and the QKT Floquet operator $\mathcal{U}_{\rm NMR}$ is subsequently applied N times to study the time evolution. An experimental circuit, showing the lineup of successive operations for simulating a QKT, is displayed in Fig. 4. The pulse sequences of this circuit for the two- and three-qubit systems used here are shown in Fig. 11 in Appendix E.

C. Measurement of $\langle J_\alpha\rangle$

In an NMR system, the direct signal measurement by quadrature detection gives $\langle I_{xi}\rangle + i\langle I_{yi}\rangle$ [49]. To extract $\langle I_{zi}\rangle$, we apply the following in succession: (i) a pulsed field gradient (PFG) which destroys the x and y magnetization components of the system and (ii) a $(\pi/2)$ pulse about the y axis to rotate the z component of magnetization to the x axis, and then detect the transverse magnetization. Note that measurement of the angular momentum components of individual spins suffices to estimate the total expectation values $\langle J_\alpha\rangle$ (see Appendix B). In the following, we discuss the results of the above-mentioned protocols for studying dynamical tunneling in two- and three-qubit spin systems.

IV. EXPERIMENTAL RESULTS

A. Tunneling in mixed phase space ($k = 3$)

As explained above, we initialize the two- and three-qubit based QKT systems to different regions of the mixed phase space at $k = 3$, and study the tunneling behavior via the scaled angular momentum components $\langle J_\alpha\rangle$ for $\alpha \in [x, y, z]$. Following Sanders and Milburn's work [37] we chose the initial state **A** (see Fig. 1) in the regular region of phase space, while the initial state **B** lies in the border between the regular region and chaotic sea. The initial state **C** lies entirely in the chaotic sea. The system was evolved for $N = 25$ kicks and $\langle J_\alpha\rangle$ was measured after each kick. Note that a classical system initialized in state **A** in the regular region is dynamically bound and cannot escape to other regions, such as the state **A**′.

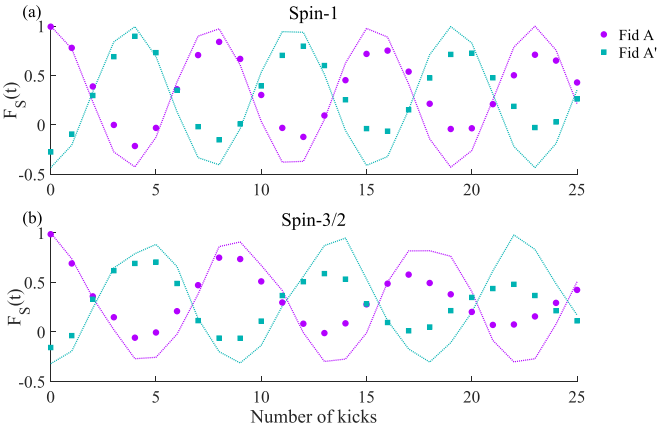

FIG. 5. Attenuated correlation of the instantaneous state of the system initialized in the regular region **A** for spin-1 (a) and spin-3/2 (b) systems with respect to the tunneling regions **A** and **A**′. Experimentally extracted values of attenuated correlation are indicated by symbols overlaid on simulated values indicated by dotted lines.

When working with such small quantum systems, the spreading of wave functions (outside the phase space region of interest) might be significant and hence needs to be monitored to ensure that tunneling we observe is not due to leakage of probability density. To quantify the overlap of the the time-evolving state with the initial coherent state in regular region **A** and the symmetry-related tunneling region **A**′, we study the trace attenuated correlation defined as [57]

$$F_{\mathbf{S}}(t) = \frac{\mathrm{Tr}[\rho(t)\rho_{\mathbf{S}}]}{\sqrt{\mathrm{Tr}[\rho(0)^2]\mathrm{Tr}\left(\rho_{\mathbf{S}}^2\right)}}, \tag{12}$$

where $\rho(t)$ is the traceless deviation density matrix of the instantaneous state of the system at time t, $\rho(0)$ is the state of the system, and ρ_S for $S \in \{\mathbf{A}, \mathrm{A}'\}$ are the deviation density matrices of coherent states **A** and **A**′. The experimentally measured (symbols) and theoretically estimated (dotted lines) attenuated correlation of systems evolving under QKT dynamics with initial state **A** are shown in Fig. 5 for spin-1 (a) and spin-3/2 (b) systems respectively. Note that the attenuated correlation can take negative values since the numerator in Eq. (12) is the product of two traceless matrices. Exact overlap is quantified by $F_{\mathbf{S}}(t) = 1$, while orthogonality is quantified by $F_{\mathbf{S}}(t) = 0$. Nonzero negative values indicate partial overlap and opposite phases between states. From Figs. 5(a) and 5(b), it is evident that the initial coherent state has maximum overlap with the regular region **A** and a modest overlap with **A**′ in spin 1 and even smaller overlap in spin 3/2. However, during the course of QKT evolution, the system gets more and more mixed, resulting in decaying overlap with both regions **A** and **A**′. The purity dynamics of the experimental two- and three-qubit systems are shown in Fig. 12 in Appendix F.

Figure 6 shows the experimental results (symbols) of scaled angular momentum components $\langle J_\alpha\rangle/j$ for a

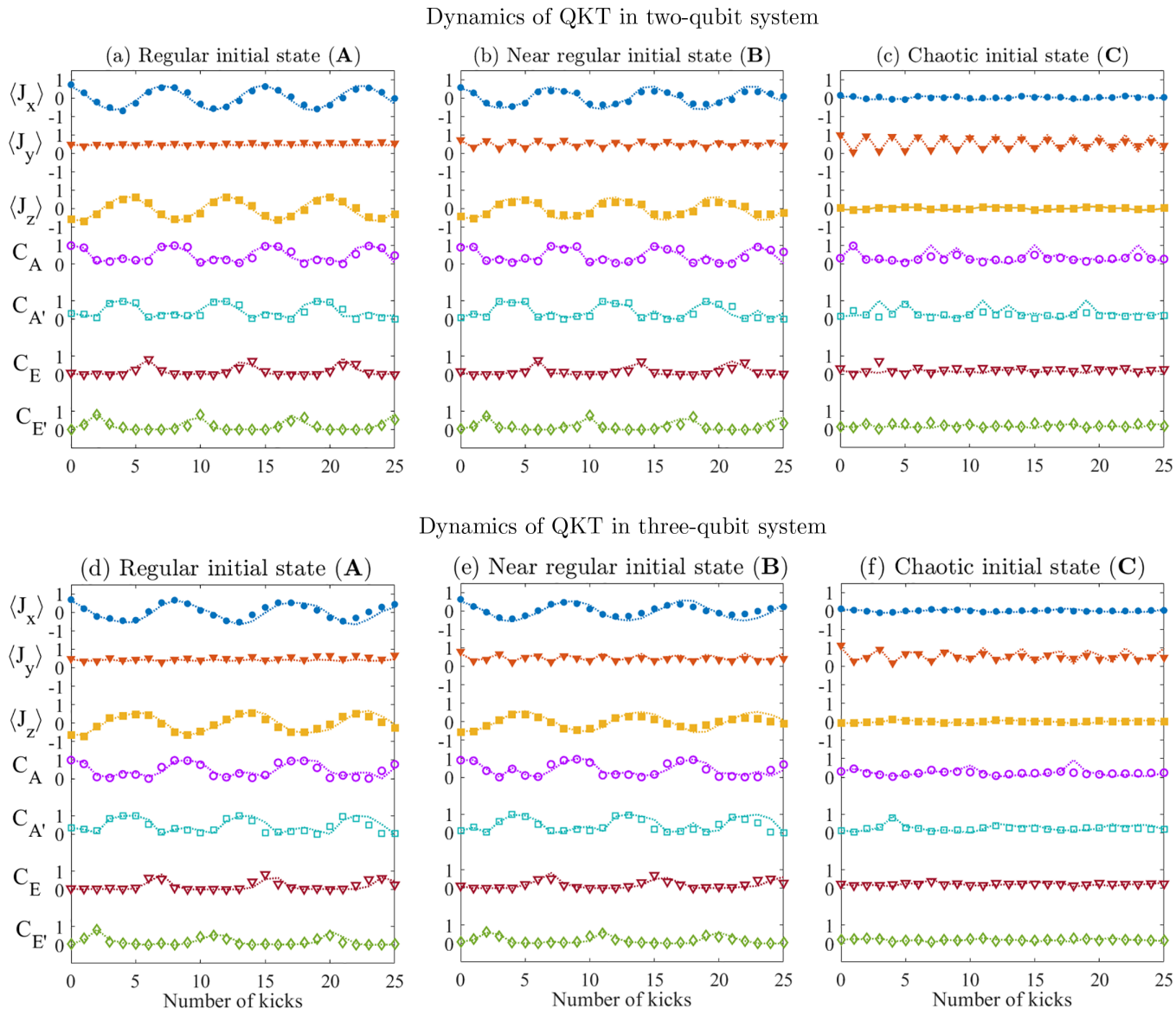

FIG. 6. Dynamics of QKT in the two-qubit spin-1 system (a)–(c) and three-qubit spin-3/2 system (d)–(f) corresponding to initialization in states **A** (a), (d), **B** (b), (e), and **C** (c), (f). The symbols indicate experimental data while dotted lines indicate simulation of the corresponding spin-j system. The upper three traces represent $\langle J_\alpha(t)\rangle$ and the lower four traces represent $C_S(t)$. In (a) and (d) we see that both the systems show clear tunneling patterns for initialization in the regular region with good agreement between simulation and experiments. The revival patterns are observed for the near-regular region as well (b), (e), but are not as prominent as those of the regular region. The patterns for the chaotic initial state (c), (f) show no clear periodicity.

spin-1 system realized using two qubits [Figs. 6(a)–6(c)] and a spin-3/2 system realized using three qubits [Figs. 6(d)–6(f)] initialized in states $\mathbf{Q} \in \{\mathbf{A}, \mathbf{B}, \mathbf{C}\}$ of the classical phase space shown in Fig. 1. The experimental data in each plot are overlaid on the corresponding simulation of single spin-j system shown by dotted lines. In all cases, we set the chaoticity parameter $k = 3$ and initialize the systems in states **A** [Figs. 6(a) and 6(d)], **B** [Figs. 6(b) and 6(e)], and **C** [Figs. 6(c) and 6(f)]. In all the graphs, the top three traces show the expectation values $\langle J_\alpha^{\mathbf{Q}}(t)\rangle$. For the initialization into state **A** in the regular region, we observe prominent oscillations in the expectation values of J_x and J_z, while that of J_y remains constant as the system is symmetric about y kicks [Figs. 6(a) and 6(d)]. A state initialized in **B** near the border of regular and chaotic regions shows similar periodicity, though not as prominent as that for **A** [Figs. 6(b) and 6(e)]. For initial state **C** in the chaotic region, we observe no clear periodicity, although the J_y component shows oscillation as the system periodically gets localized and delocalized with kicks [Figs. 6(c) and 6(f)]. The experimental data show a decay in the oscillations due to decoherence and other experimental imperfections. We note a relatively longer time period of three-qubit oscillations compared to that of the two-qubit system (see Appendix D for further analysis).

In all the plots, the lowest four traces show correlations

$$C_{\mathbf{S}}(t) = |\langle J^{\mathbf{S}} | J^{\mathbf{Q}}(t)\rangle|^2 \tag{13}$$

between $J^{\mathbf{S}}$ of state **S** and the instantaneous total angular momentum operators $J^{\mathbf{Q}}(t)$. The overlap measure allows us

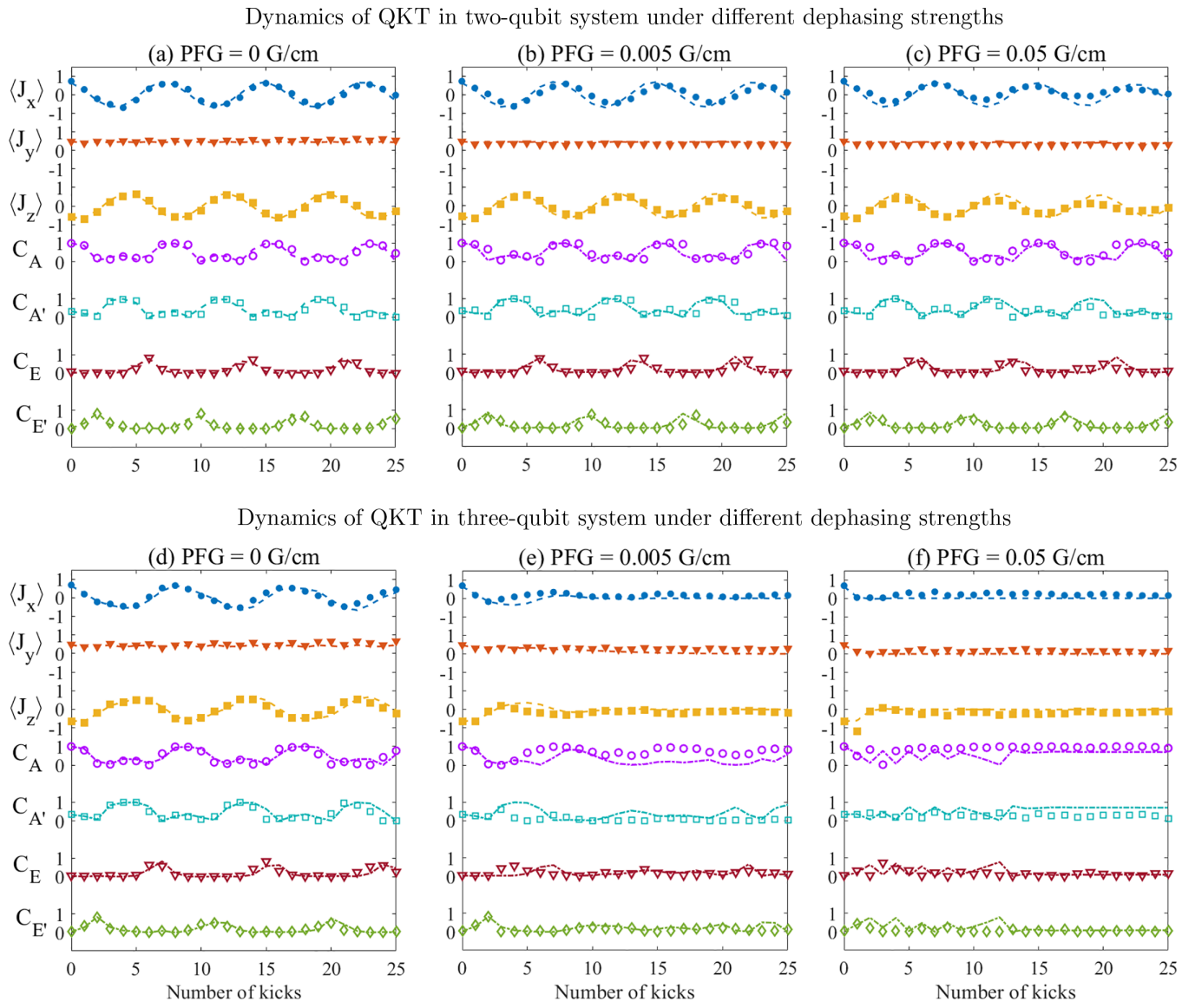

FIG. 7. Effects of dephasing noise on dynamical tunneling in two qubits (a)–(c) as well as three qubits (d)–(f), with PFG strengths 0 G/cm (a), (d), 0.005 G/cm (b), (e), and 0.05 G/cm (c), (f). In all the cases, the system was initialized in state **A** inside a regular region of Fig. 1. The symbols indicate experimental data overlaid on dashed lines corresponding to simulations of two- and three-qubit systems with dephasing noise. The upper three traces represent $\langle J_\alpha(t)\rangle$ and the lower four traces represent $C_S(t)$. While both the systems are susceptible to dephasing noise the two-qubit system is relatively more robust in comparison to the three-qubit system wherein the oscillations have decayed more severely with noise.

to track the localization of the system in states **A** and **A**′ as it tunnels between these regular regions. As expected, when the system is initialized in state **A**, we see clear periodic and out-of-phase tunneling oscillations of $C_{\mathbf{A}(\mathbf{A}')}(t)$ [Figs. 6(a) and 6(d)]. These tunneling oscillations persist even for near-regular initialization in state **B** due to significant spreading of the low dimensional quantum systems considered here [Figs. 6(b) and 6(e)]. However, such tunneling oscillations are washed out for chaotic initialization in state **C** [Figs. 6(c) and 6(f)]. Furthermore, the correlation measures $C_{\mathbf{S}}(t)$ indicate that for the chaotic state, it is widely delocalized. The bottom two traces in Fig. 6 capture brief leakage amplitudes to the regions **E** and **E**′, which is the consequence of deep-quantum systems considered here.

B. Robustness of dynamical tunneling

Now that we observe tunneling across a dynamical barrier, it is interesting to see the role of quantum coherence in sustaining tunneling. To this end, we monitor the robustness of dynamical tunneling between regular regions **A** and **A**′ under dephasing noise. For this purpose, we use PFGs which introduce a linearly varying magnetic field along the z direction and accordingly distribute Larmor frequencies over the length of the sample [50]. PFGs along with translational diffusion of molecules effectively induce strong dephasing in the system [58,59]. The experimental impact of dephasing on dynamical tunneling is shown in Fig. 7 for two-qubit [Figs. 7(a)–7(c)] and three-qubit systems [Figs. 7(d)–7(f)] and for PFG strengths 0 G/cm [Figs. 7(a) and 7(d)], 0.005 G/cm

[Figs. 7(b) and 7(e)], and 0.05 G/cm [Figs. 7(c) and 7(f)]. The 0-G/cm scenario in Figs. 7(a) and 7(d) is the same as Figs. 6(a) and 6(d) and has been replotted here for visual comparison. Here, the experimental data (symbols) are overlaid on numerical simulations (dashed lines) of two- and three-qubit systems with dephasing effects instead of the corresponding single spin-j systems. We find that in both cases, the tunneling behavior is weakened by dephasing noise. In the two-qubit system, the periodic oscillations survive, but with decaying tunneling amplitudes [Figs. 7(b) and 7(c)]. In the three-qubit case, even in the presence of weak PFG of 0.005 G/cm the oscillations decay much faster [Figs. 7(e) and 7(f)]. Here, the correlation measure indicates that the system has a preferentially larger overlap with the regular region **A** compared to other regular regions. We can also see that the simulation of experimental data agrees reasonable well with the actual data. The difference seen between them can be attributed to the effects of other imperfections such as gradient and rf calibration, and rf inhomogeneity. These results indicate the fragility of dynamical tunneling under dephasing noise, and thereby establish the importance of quantum coherence in sustaining the phenomenon.

V. SUMMARY AND OUTLOOK

Dynamical tunneling, such as chaos-assisted tunneling, is a well-studied phenomenon and has been demonstrated experimentally in driven cold atomic clouds and microwave annular billiards, and has most recently been used to generate NOON states [33]. However, a systematic study of tunneling with system size and different initial conditions was not available. In this paper, we have experimentally demonstrated chaos-assisted tunneling in two- and three-qubit systems using a NMR based testbed. We initialized the systems to different regions of the phase space—regular, near regular, (the border region between regular and chaotic), and chaotic. Following Ref. [37], we use $\langle J_\alpha \rangle$, the components of the angular momentum operator, as probes to study dynamical tunneling. We observe that the systems initialized in the regular region show periodic oscillation in $\langle J_\alpha \rangle$. Systems initialized in the near-regular region also show periodicity in $\langle J_\alpha \rangle$, but the oscillations are not as perfect as those for the case of the initial state in a regular region. Further, systems initialized in a chaotic region show no periodicity. Additionally, by analyzing the norm distance between the instantaneous total angular momentum operator and that corresponding to either of the regular regions, we monitor the periodic tunneling of the system between these regions for different initial conditions.

To understand the significance of quantum coherence in maintaining dynamical tunneling, we studied the robustness of tunneling against dephasing noise. Experimental results showed that while both the spin $j = 1$ and $3/2$ systems are susceptible to dephasing noise, the effect was severe for the larger system, wherein the revivals of $\langle J_\alpha \rangle$ were almost completely destroyed in the presence of dephasing noise.

Tunneling suppression for increasing number of qubits will be related to the $\hbar$ scaling in the kicked top model. For the QKT, quantum correlations are known to decay in a power-law form as a function of $\hbar$ [48]. It will be useful to explore the validity of this prediction for dynamical tunneling in future studies. This is likely to be a challenging exercise from an experimental point of view since it will require maintaining coherence with a large number of interacting spins. Systems with all-to-all and effectively equal spin couplings enable convenient simulation of the nonlinear evolution under J_z^2. Since such coupling architectures are difficult to find, this poses a challenge in experimentally simulating the kicked top model of large spin-j systems. In heteronuclear systems with unequally coupled spins, the nonlinear evolution with an effective uniform coupling can be realized with the help of spin-selective refocusing pulses as shown here. However, we needed individual experiments to detect magnetization of each heteronuclear species. One can also use a homonuclear spin system which allows detecting magnetization of all spins in a single experiment, but realizing spin-selective pulses becomes difficult. Moreover, in homonuclear systems, the chemical shift evolution will also need to be refocused.

Further, while it might not be entirely surprising that introduction of noise kills tunneling effects, there are Floquet engineering techniques that allow calibrated disorder while still suppressing decoherence [60,61]. It will be interesting to explore if such Floquet schemes help sustain chaos-assisted tunneling even in the presence of noise. Another interesting topic to consider would be a scenario of quantum tunneling in the simultaneous presence of a potential-energy barrier as well as a dynamical barrier. These aspects will be considered in a later work.

ACKNOWLEDGMENTS

The authors acknowledge valuable discussions with Prof. A Lakshminarayan, C. Alexander, and A. Chatterjee. We thank Dr. S. Aravinda for his inputs on improving the paper. M.S.S. acknowledges MATRICS Grant No. MTR/2019/001111 from SERB, DST, Government of India. T.S.M. acknowledges funding from DST/ICPS/QuST/2019/Q67. We thank NMICPS funding from the DST, Government of India through the I-HUB QTF, IISER-Pune.

APPENDIX A: WAVE-FUNCTION SPREADING IN THE DEEP-QUANTUM LIMIT

In the deep-quantum limit, it is important to take into account the spread or finite width of spin wave functions. The spin coherent state into which the system is initialized has a finite spread depending on the spin size, which for smaller spins is more than that of a larger spin. Let us now look at the extent of overlap between states localized in regions **A** and **A**′. Figure 8 shows the theoretical attenuated correlation computed using Eq. (12) of the instantaneous state of a system initialized in **A** and undergoing QKT dynamics for $k = 3$ for spin-1 (a), spin-5 (b), and spin-20 (c) systems. It is evident that as the system size increases, the degree of overlap of states localized in **A**(**A**′) with **A**′(**A**) decreases. This behavior also emphasizes the importance of chaotic states in dynamical tunneling. As the system size increases, the overlap of a localized state in a regular region (**A**,**A**′) with the surrounding chaotic state decreases, which in turn hampers the tunneling efficiency as is reflected in the prolonged

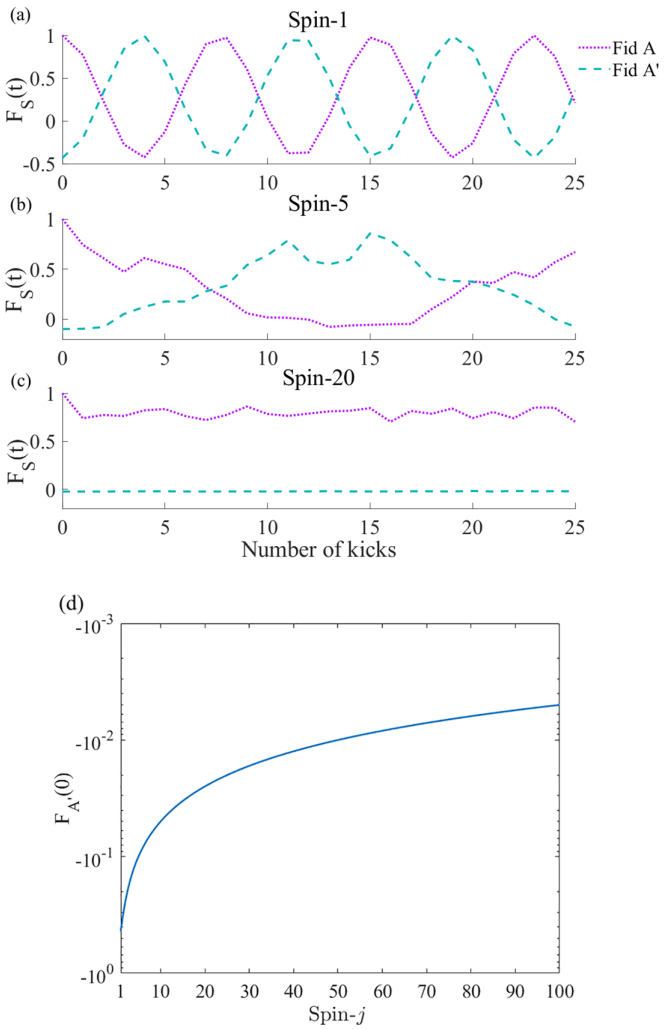

FIG. 8. Attenuated correlation of the instantaneous state of QKT with $k = 3$ initialized in the regular region **A** for spin-1 (a) and spin-5 (b) and spin-20 (c) systems with respect to the tunneling regions **A** (dotted lines) and **A**′ (dashed lines). Attenuated correlation of coherent state **A** with **A**′, as a function of spin-j size (d).

time periods in Figs. 8(b) and 8(c). The attenuated correlation of a single spin-j system in coherent state **A** with the corresponding state **A**′ as a function of spin size is shown in Fig. 8(d). It can be seen that to achieve overlap <0.1 between **A** and **A**′, we need at least spin 5, i.e., ten qubits, while overlap <0.01 requires at least spin 50 (or 100 qubits), which is beyond the reach of current state-of-the-art quantum simulators.

APPENDIX B: MEASUREMENT OF EXPECTATION VALUES $\langle J_\alpha \rangle$

The general state ρ of the multiqubit system can be expanded in the product operator basis of constituent spins as

$$\rho = \frac{\mathbb{1}}{2^n} + \sum_i c_{\alpha i} I_{\alpha i} + \sum_{ij\alpha\beta} c_{\alpha\beta ij} I_{\alpha i} I_{\beta j} + \cdots, \tag{B1}$$

where higher-order spin correlation terms are not shown. The total expectation value $\langle J_\alpha \rangle$ for the linear term can then be

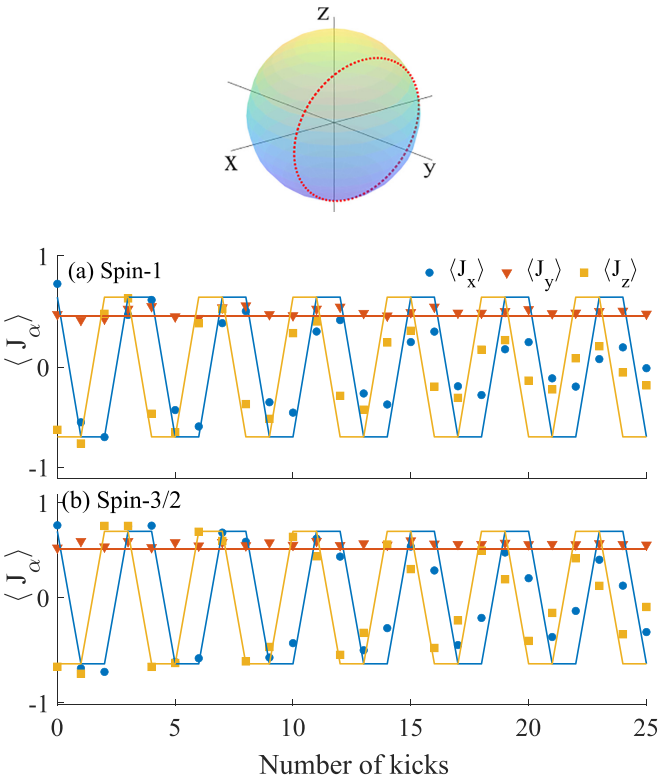

FIG. 9. Control experiments with $k = 0$ for the two- and three-qubit systems. (a) Denotes the classical trajectory for different initial states. (b) Shows the data of $\langle J_\alpha \rangle$ for $\alpha \in \{x, y, z\}$ from two- and three-qubit systems respectively. The symbols indicate experimental data, while solid lines indicate simulations. We can see that the experimental data are in good agreement with simulated data. The decay in experimental data points is due to relaxation in the systems.

estimated as

$$\langle J_\alpha \rangle = \mathrm{Tr}\left[\rho \sum_i I_{\alpha i}\right] = \sum_i c_{\alpha i} I_{\alpha i} = \sum_i \mathrm{Tr}[\rho_i I_{\alpha i}], \tag{B2}$$

where $\rho_i = \frac{\mathbb{1}}{2} + \sum_i c_{\alpha i} I_{\alpha i}$ are the reduced density matrices of the constituent spin systems.

APPENDIX C: $k = 0$ CONTROL EXPERIMENTS

As a control, we first studied the behavior of the system in the absence of chaos, i.e., $k = 0$. In this case, the system just evolves under $(\pi/2)$ kicks applied about the y axis. The classical equations of motion [Eq. (3)] at the $(N + 1)$th kick relate to the Nth kick as follows:

$$\begin{aligned} X(N+1) &= Z(N), \\ Y(N+1) &= Y(N), \\ Z(N+1) &= -X(N). \end{aligned} \tag{C1}$$

The y component of the system remains invariant under evolution, while the x and z components evolve with each kick. The evolution is thus restricted to circles in the xz plane for any given initial state. The results of this control experiment are displayed in Fig. 9 for the system initialized into the phase space region characterized by $|\theta, \phi\rangle = (2.25, 0.63)$.

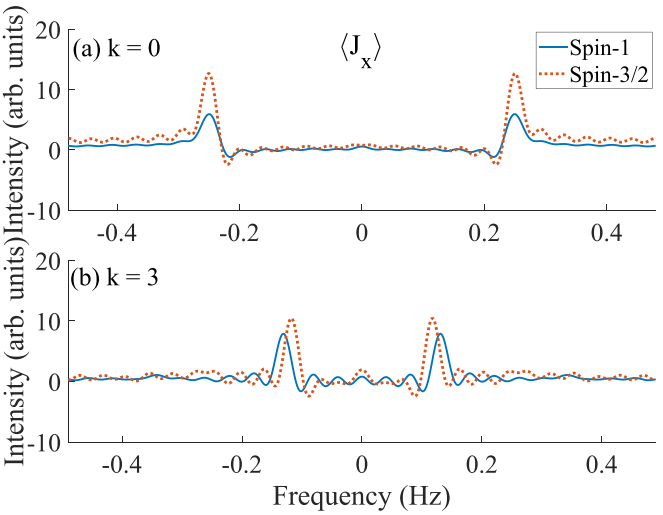

FIG. 10. Fourier transform of (a) control experiments and (b) tunneling experiments for spin-1 (solid lines) and spin-3/2 (dotted lines) systems. We can see that in the case of control experiments, the frequency of oscillation is the same for both the systems. In the case of tunneling experiments, there is a clear shift in the frequency of the three-qubit system as compared to the two-qubit system. This is in accordance with the expectation that as system size increases the tunneling effect should get suppressed.

The experimental data show a decay in the amplitude of the oscillation due to accumulation of pulse errors with each kick. We can see that both the two- and three-qubit systems have oscillating J_x and J_z values, while the value of J_y remains constant. Moreover, the period of oscillation is the same in both cases. To understand the frequency of oscillations better, we computed the Fourier transform of the time evolution of the system. The frequency domain analysis of the evolution [displayed in Fig. 10(a)] shows that the period of oscillation, as anticipated, is independent of the system size.

APPENDIX D: TIME PERIOD OF OSCILLATIONS AND SYSTEM SIZE DEPENDENCE

Comparing the periodicity of oscillation, we can see that the period is slightly longer for the three-qubit system which completes about three oscillations in 25 kicks, while the two-qubit system completes three and a half oscillations in the same duration. In the case of $k = 3$, the period of oscillations decreases with increasing system size. This is clear from the frequency domain picture shown in Fig. 10. This is expected since as the system size increases, it approaches the classical limit, thereby suppressing quantum behavior.

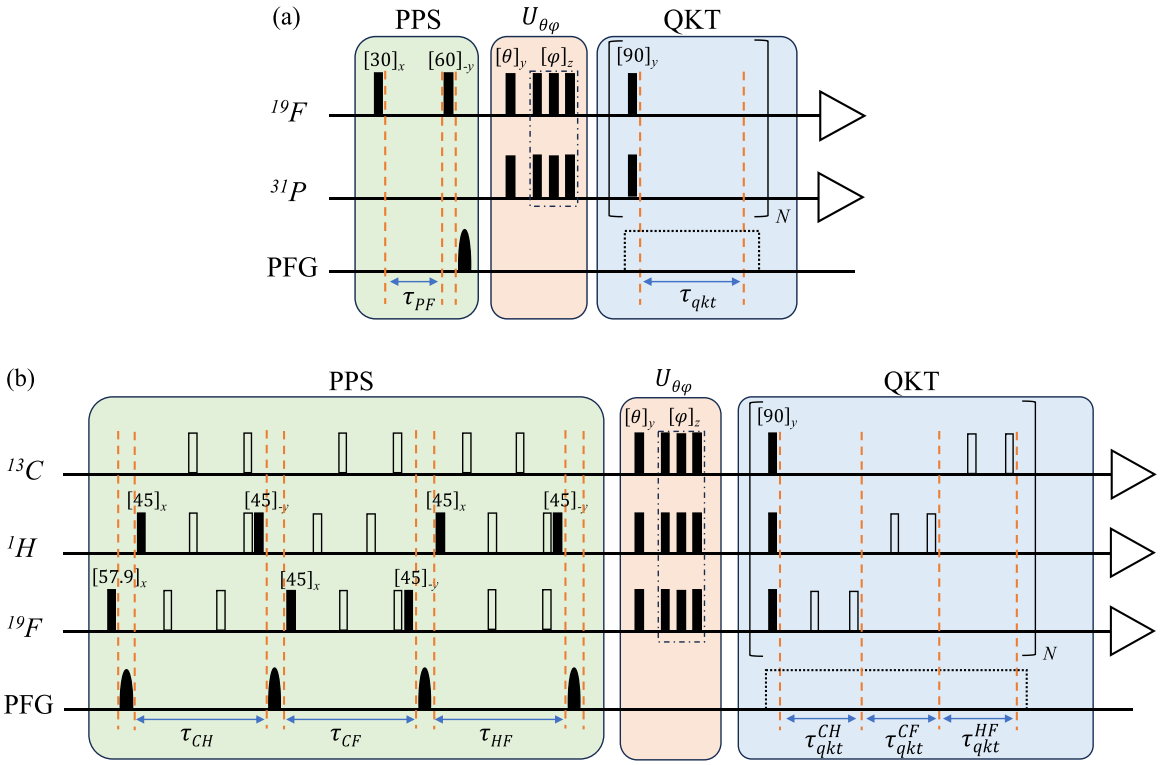

FIG. 11. Pulse sequences for simulating QKT dynamics in (a) the two-qubit register in the sodium fluorophosphate molecule with $\tau_{PF} = 1/(2\mathcal{J}_{PF})$, $\tau_{QKT} = 3/(2\pi\mathcal{J}_{FP})$ and (b) the three-qubit register in dibromofluoromethane with $\tau_{CH} = 1/(2\mathcal{J}_{CH})$, $\tau_{CF} = 2/|\mathcal{J}_{CF}| - 1/2|\mathcal{J}_{CF}|$ (to take care of the negative sign of $\mathcal{J}_{CF}$) and $\tau_{HF} = 1/(2\mathcal{J}_{HF})$, and $\tau_{QKT}^{CH} = 1/(\pi\mathcal{J}_{CH})$, $\tau_{QKT}^{CF} = 2/|\mathcal{J}_{CF}| - 1/|\pi\mathcal{J}_{CF}|$ (to take care of negative coupling), $\tau_{QKT}^{HF} = 1/(\pi\mathcal{J}_{HF})$. The solid rectangles represent rotations by an angle and about an axis as indicated over them, while the blank rectangles represent π pulses to refocus the evolution under undesired spin-spin interaction. The $[\phi]_z$ rotation in both cases was effectively realized using three pulses $[90]_y[\phi]_x[90]_{-y}$ (time ordered from left to right). The black half ellipsoids and dotted rectangles represent PFG along the $+z$ axis. The dotted rectangles in PFG are only applied in dephasing experiments. The right triangles at the end of the pulse sequences represent FID in each nuclear species.

APPENDIX E: PPS AND QKT PULSE SEQUENCES

The pulse sequences for PPS preparation and QKT dynamics in two- and three-qubit systems are shown in Figs. 11(a) and 11(b) respectively.

The dynamics of the systems evolving under the QKT Hamiltonian is as given in Eq. (2). The nonlinear Hamiltonian $H_{\rm NL} = \frac{k}{2j\tau}J_z^2$ is evolved for time τ which gives the unitary $U = \exp(-iH_{\rm NL}\tau)$. The expansion of the nonlinear term for a system of $2j$ qubits emulating the dynamics of a single spin-j system is shown in Eq. (8). Following this expansion, we can see that the main parameter governing the dynamics of the nonlinear term is the chaoticity parameter k.

In the experimental systems, we evolve the spin-1 and spin-3/2 systems under their spin-spin coupling Hamiltonians [Eq. (4)] for appropriate durations, to achieve the desired chaoticity parameter value k. Comparing the nonlinear term of the QKT Hamiltonian [Eq. (8)] with the spin-spin coupling NMR Hamiltonian [Eq. (4)], for a two-qubit system we get $[\{k/(2j\tau)\}2I_{z1}I_{z2}]\tau \equiv \pi\mathcal{J}_{\rm FP}2I_{zF}I_{zP}\tau_{\rm QKT}$, which gives the condition $k/(2j) \equiv \pi\mathcal{J}_{\rm FP}\tau_{\rm QKT}$. Hence the time for which evolution under coupling term is required to realize a chaoticity parameter value k is $\tau_{\rm QKT} = k/(2\pi j\mathcal{J}_{\rm FP})$.

For the three-qubit system, a similar calculation gives

$$\frac{k}{2j\tau}(2I_{z1}I_{z2} + 2I_{z2}I_{z3} + 2I_{z1}I_{z3})\tau \equiv 2\pi\left(\mathcal{J}_{\rm CH}\tau_{\rm QKT}^{\rm CH}I_{zC}I_{zH} + \mathcal{J}_{\rm CF}\tau_{\rm QKT}^{\rm CF}I_{zC}I_{zF} + \mathcal{J}_{\rm HF}\tau_{\rm QKT}^{\rm HF}I_{zH}I_{zF}\right), \tag{E1}$$

which describes the condition for the respective evolution times $\tau_{\rm QKT}^{\rm CH}$, $\tau_{\rm QKT}^{\rm CF}$, and $\tau_{\rm QKT}^{\rm HF}$. The explicit forms of these durations are also mentioned in the caption of Fig. 11. Hence, the dynamics is primarily determined by the k value, and evolution under intrinsic system parameters in experiments is tailored accordingly.

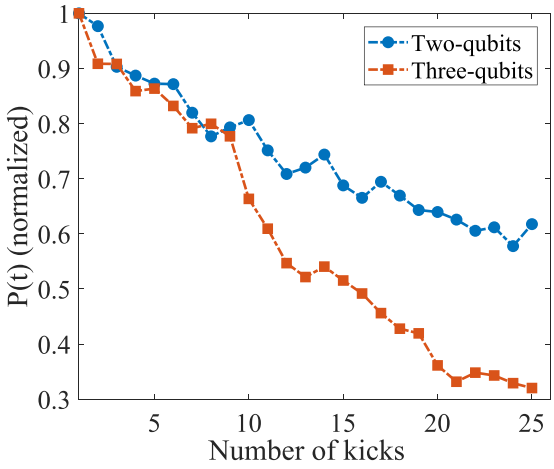

FIG. 12. Experimental normalized purity function $P(t)$ of two- and three-qubit systems during QKT evolution, denoted by filled circles and squares respectively. The faster decay of purity in the three-qubit system in comparison to the two-qubit system is clearly evident.

In our experiments, for $k = 3$ the effective delay between the kicks $\tau_{\rm QKT}$ was set to 5.5×10^{-4} and 132×10^{-4} s in two- and three-qubit systems respectively. For 25 kicks ($N = 25$ in Fig. 11), these amounted to experimental durations of 0.014 and 0.3 s in the two- and three-qubit systems respectively.

APPENDIX F: PURITY DYNAMICS

To understand the degree of mixedness in the experimental system as it evolves under QKT dynamics, we study the purity, defined by $P(t) = {\rm Tr}(\rho(t)^2)$, where $\rho(t)$ is the instantaneous traceless deviation density matrix of the state at time t. The behavior of the normalized purity function is shown in Fig. 12. We can see that both systems become more mixed during the course of QKT evolution. However, the three-qubit system suffers a significantly higher loss of purity in comparison to the two-qubit system, as is evident from Fig. 12.

[1] D. J. Griffiths and D. F. Schroeter, *Introduction to Quantum Mechanics* (Cambridge University Press, New York, 2018).

[2] B. Josephson, Possible new effects in superconductive tunnelling, Phys. Lett. **1**, 251 (1962).

[3] S. Shapiro, Josephson Currents in Superconducting Tunneling: The Effect of Microwaves and Other Observations, Phys. Rev. Lett. **11**, 80 (1963).

[4] M. Tinkham, *Introduction to Superconductivity* (Courier, New York, 2004).

[5] P. Bedrossian, D. Chen, K. Mortensen, and J. Golovchenko, Demonstration of the tunnel-diode effect on an atomic scale, Nature (London) **342**, 258 (1989).

[6] E. Mevel, P. Breger, R. Trainham, G. Petite, P. Agostini, A. Migus, J.-P. Chambaret, and A. Antonetti, Atoms in Strong Optical Fields: Evolution from Multiphoton to Tunnel Ionization, Phys. Rev. Lett. **70**, 406 (1993).

[7] J. Ankerhold, *Quantum Tunneling in Complex Systems: The Semiclassical Approach*, Springer Tracts in Modern Physics Vol. 224 (Springer, New York, 2007).

[8] J. Chen, *Introduction to Scanning Tunneling Microscopy*, 3rd ed., Monographs on the Physics and Chemistry of Materials, Vol. 69 (Oxford University Press, New York, 2021).

[9] S. Tomsovic and D. Ullmo, Chaos-assisted tunneling, Phys. Rev. E **50**, 145 (1994).

[10] S. Keshavamurthy and P. Schlagheck, *Dynamical Tunneling: Theory and Experiment* (CRC Press, Boca Raton, FL, 2011).

[11] R. Lawton and M. Child, Excited stretching vibrations of water: the quantum mechanical picture, Mol. Phys. **40**, 773 (1980).

[12] R. Lawton and M. Child, Local and normal stretching vibrational states of H2O, Mol. Phys. **44**, 709 (1981).

[13] M. J. Davis and E. J. Heller, Quantum dynamical tunneling in bound states, J. Chem. Phys. **75**, 246 (1981).

[14] E. J. Heller and M. J. Davis, Quantum dynamical tunneling in large molecules: A plausible conjecture, J. Phys. Chem. **85**, 307 (1981).

[15] A. Peres, Dynamical Quasidegeneracies and Quantum Tunneling, Phys. Rev. Lett. **67**, 158 (1991).

[16] S. Tomsovic, Tunneling and chaos, Phys. Scr. **T90**, 162 (2001).
[17] O. Brodier, P. Schlagheck, and D. Ullmo, Resonance-Assisted Tunneling in Near-Integrable Systems, Phys. Rev. Lett. **87**, 064101 (2001).
[18] A. Bäcker, R. Ketzmerick, S. Löck, M. Robnik, G. Vidmar, R. Höhmann, U. Kuhl, and H.-J. Stöckmann, Dynamical Tunneling in Mushroom Billiards, Phys. Rev. Lett. **100**, 174103 (2008).
[19] O. Brodier, P. Schlagheck, and D. Ullmo, Resonance-assisted tunneling, Ann. Phys. (NY) **300**, 88 (2002).
[20] S. Löck, A. Bäcker, R. Ketzmerick, and P. Schlagheck, Regular-to-Chaotic Tunneling Rates: From the Quantum to the Semiclassical Regime, Phys. Rev. Lett. **104**, 114101 (2010).
[21] C. Eltschka and P. Schlagheck, Resonance- and Chaos-Assisted Tunneling in Mixed Regular-Chaotic Systems, Phys. Rev. Lett. **94**, 014101 (2005).
[22] S. Gehler, S. Löck, S. Shinohara, A. Bäcker, R. Ketzmerick, U. Kuhl, and H.-J. Stöckmann, Experimental Observation of Resonance-Assisted Tunneling, Phys. Rev. Lett. **115**, 104101 (2015).
[23] F. Fritzsch, R. Ketzmerick, and A. Bäcker, Resonance-assisted tunneling in deformed optical microdisks with a mixed phase space, Phys. Rev. E **100**, 042219 (2019).
[24] S. Keshavamurthy, Resonance-assisted tunneling in three degrees of freedom without discrete symmetry, Phys. Rev. E **72**, 045203(R) (2005).
[25] S. Keshavamurthy, Dynamical tunnelling in molecules: Quantum routes to energy flow, Int. Rev. Phys. Chem. **26**, 521 (2007).
[26] C. Dembowski, H.-D. Gräf, A. Heine, R. Hofferbert, H. Rehfeld, and A. Richter, First Experimental Evidence for Chaos-Assisted Tunneling in a Microwave Annular Billiard, Phys. Rev. Lett. **84**, 867 (2000).
[27] D. A. Steck, W. H. Oskay, and M. G. Raizen, Observation of chaos-assisted tunneling between islands of stability, Science **293**, 274 (2001).
[28] D. A. Steck, W. H. Oskay, and M. G. Raizen, Fluctuations and Decoherence in Chaos-Assisted Tunneling, Phys. Rev. Lett. **88**, 120406 (2002).
[29] W. K. Hensinger, H. Häffner, A. Browaeys, N. R. Heckenberg, K. Helmerson, C. McKenzie, G. J. Milburn, W. D. Phillips, S. L. Rolston, H. Rubinsztein-Dunlop *et al.*, Dynamical tunnelling of ultracold atoms, Nature (London) **412**, 52 (2001).
[30] A. Mouchet, C. Miniatura, R. Kaiser, B. Grémaud, and D. Delande, Chaos-assisted tunneling with cold atoms, Phys. Rev. E **64**, 016221 (2001).
[31] R. Hofferbert, H. Alt, C. Dembowski, H.-D. Gräf, H. L. Harney, A. Heine, H. Rehfeld, and A. Richter, Experimental investigations of chaos-assisted tunneling in a microwave annular billiard, Phys. Rev. E **71**, 046201 (2005).
[32] G. Vanhaele and P. Schlagheck, NOON states with ultracold bosonic atoms via resonance- and chaos-assisted tunneling, Phys. Rev. A **103**, 013315 (2021).
[33] G. Vanhaele, A. Bäcker, R. Ketzmerick, and P. Schlagheck, Creating triple-NOON states with ultracold atoms via chaos-assisted tunneling, Phys. Rev. A **106**, L011301 (2022).
[34] U. Satpathi, S. Ray, and A. Vardi, Chaos-assisted many-body tunnelling, Phys. Rev. E **106**, L042204 (2022).
[35] F. Haake, M. Kuś, and R. Scharf, Classical and quantum chaos for a kicked top, Z. Phys. B **65**, 381 (1987).
[36] S. Chaudhury, A. Smith, B. Anderson, S. Ghose, and P. S. Jessen, Quantum signatures of chaos in a kicked top, Nature (London) **461**, 768 (2009).
[37] B. Sanders and G. Milburn, The effect of measurement on the quantum features of a chaotic system, Z. Phys. B **77**, 497 (1989).
[38] S. Dogra, V. Madhok, and A. Lakshminarayan, Quantum signatures of chaos, thermalization, and tunneling in the exactly solvable few-body kicked top, Phys. Rev. E **99**, 062217 (2019).
[39] D. G. Cory, R. Laflamme, E. Knill, L. Viola, T. Havel, N. Boulant, G. Boutis, E. Fortunato, S. Lloyd, R. Martinez *et al.*, NMR based quantum information processing: Achievements and prospects, Fortschr. Phys. **48**, 875 (2000).
[40] D. Suter and T. Mahesh, Spins as qubits: Quantum information processing by nuclear magnetic resonance, J. Chem. Phys. **128**, 052206 (2008).
[41] A. G. Araujo-Ferreira, R. Auccaise, R. S. Sarthour, I. S. Oliveira, T. J. Bonagamba, and I. Roditi, Classical bifurcation in a quadrupolar NMR system, Phys. Rev. A **87**, 053605 (2013).
[42] V. R. Krithika, V. S. Anjusha, U. T. Bhosale, and T. S. Mahesh, NMR studies of quantum chaos in a two-qubit kicked top, Phys. Rev. E **99**, 032219 (2019).
[43] V. R. Krithika, P. Solanki, S. Vinjanampathy, and T. S. Mahesh, Observation of quantum phase synchronization in a nuclear-spin system, Phys. Rev. A **105**, 062206 (2022).
[44] X. Peng, J. Du, and D. Suter, Quantum phase transition of ground-state entanglement in a Heisenberg spin chain simulated in an NMR quantum computer, Phys. Rev. A **71**, 012307 (2005).
[45] E. M. Fortes, I. García-Mata, R. A. Jalabert, and D. A. Wisniacki, Signatures of quantum chaos transition in short spin chains, Europhys. Lett. **130**, 60001 (2020).
[46] X. Nie, B.-B. Wei, X. Chen, Z. Zhang, X. Zhao, C. Qiu, Y. Tian, Y. Ji, T. Xin, D. Lu, and J. Li, Experimental Observation of Equilibrium and Dynamical Quantum Phase Transitions via Out-of-Time-Ordered Correlators, Phys. Rev. Lett. **124**, 250601 (2020).
[47] J. Li, R. Fan, H. Wang, B. Ye, B. Zeng, H. Zhai, X. Peng, and J. Du, Measuring Out-of-Time-Order Correlators on a Nuclear Magnetic Resonance Quantum Simulator, Phys. Rev. X **7**, 031011 (2017).
[48] U. T. Bhosale and M. S. Santhanam, Signatures of bifurcation on quantum correlations: Case of the quantum kicked top, Phys. Rev. E **95**, 012216 (2017).
[49] M. H. Levitt, *Spin Dynamics: Basics of Nuclear Magnetic Resonance* (Wiley, New York, 2013).
[50] J. Cavanagh, W. J. Fairbrother, A. G. Palmer III, and N. J. Skelton, *Protein NMR Spectroscopy: Principles and Practice* (Elsevier, Amsterdam, 1995).
[51] X. Wang, S. Ghose, B. C. Sanders, and B. Hu, Entanglement as a signature of quantum chaos, Phys. Rev. E **70**, 016217 (2004).
[52] J. M. Radcliffe, Some properties of coherent spin states, J. Phys. A **4**, 313 (1971).
[53] J. R. Klauder and B. Skagerstam, *Coherent States: Applications in Physics and Mathematical Physics* (World Scientific, Singapore, 1985).

[54] D. G. Cory, A. F. Fahmy, and T. F. Havel, Ensemble quantum computing by NMR spectroscopy, Proc. Natl. Acad. Sci. USA **94**, 1634 (1997).

[55] N. A. Gershenfeld and I. L. Chuang, Bulk spin-resonance quantum computation, Science **275**, 350 (1997).

[56] V. R. Krithika, S. Pal, R. Nath, and T. S. Mahesh, Observation of interaction induced blockade and local spin freezing in a NMR quantum simulator, Phys. Rev. Res. **3**, 033035 (2021).

[57] E. M. Fortunato, M. A. Pravia, N. Boulant, G. Teklemariam, T. F. Havel, and D. G. Cory, Design of strongly modulating pulses to implement precise effective Hamiltonians for quantum information processing, J. Chem. Phys. **116**, 7599 (2002).

[58] W. S. Price, Pulsed-field gradient nuclear magnetic resonance as a tool for studying translational diffusion. Part 1: Basic theory, Concepts Magn. Reson. **9**, 299 (1997).

[59] A. Shukla, M. Sharma, and T. Mahesh, NOON states in star-topology spin-systems: Applications in diffusion studies and RF inhomogeneity mapping, Chem. Phys. Lett. **592**, 227 (2014).

[60] C. Chen, J.-H. An, H.-G. Luo, C. P. Sun, and C. H. Oh, Floquet control of quantum dissipation in spin chains, Phys. Rev. A **91**, 052122 (2015).

[61] P. W. Claeys, M. Pandey, D. Sels, and A. Polkovnikov, Floquet-Engineering Counterdiabatic Protocols in Quantum Many-Body Systems, Phys. Rev. Lett. **123**, 090602 (2019).